Check for updates

Inhibitory behaviour and adsorption stability of benzothiazole derivatives as corrosion inhibitors towards galvanised steel†

Qiushi Deng, [iD] *[a] José María Castillo-Robles,[ab] Ernane de Freitas Martins, [iD] [b]
Pablo Ordejón, [iD] [b] Jan-Niclas Gorges,[c] Philipp Eiden,[c] Xiao-Bo Chen, [iD] [a]
Patrick Keil [iD] *[ad] and Ivan Cole*[a]

An in-depth understanding of corrosion inhibitor behaviour(s) at the metal–solution interface governed by unique molecular features is the key premise to realising molecular tailoring for pronounced metal protection. This study investigated the distinct adsorption behaviours induced by merely replacing the chemical functionality upon benzothiazole, *i.e.*, 2-mercaptobenzothiazole (2-MBT) and 2-aminobenzothiazole (2-ABT), towards electro-galvanised steel (ZE) corrosion using both experimental and theoretical approaches. Electrochemical results confirm that both inhibitor candidates act as corrosion inhibitors for ZE in NaCl solution. The underlying interactions of the inhibitor molecule with the targeting metal, dissolved metal ions and corrosion products were explored by means of X-ray photoelectron spectroscopy, focused ion beam scanning electron microscopy and Raman spectroscopy. It is suggested that 2-MBT facilitates the precipitation upon the ZE by complexing with the released Zn^{2+} in solution, while 2-ABT promotes preferentially thin inhibitor film formation initiated by chemisorption. Density functional theory (DFT) reveals that at high concentrations the molecules tend to adsorb vertically (slightly tilted) at the surface, where the presented heteroatoms enhance surface–molecule interaction. In addition, DFT suggests that the strong binding strength of 2-MBT could facilitate the formation of complexes with displaced Zn. Based on the proposed mechanisms, the adsorption stability upon polarised ZE surfaces was determined, which reveals that 2-MBT forms a thick inhibitor layer at a relatively high polarisation state, whereas 2-ABT dissociates from the surface with the increasing value of surface overpotential. The findings of this study provide structural understanding that underpins inhibitor tailoring and molecular design to achieve the desired inhibition properties.

Design, System, Application

Performance-driven molecular design of corrosion inhibitors has attracted appreciable attention to facilitate high-efficiency inhibitive system design against metal corrosion. The efficiency of corrosion inhibition is, in principle, associated with the presented chemical functionalities of inhibitor molecules interacting with the targeting metal and the subsequent formation of surface protective film. Nonetheless, the structure–property correlation remains far from comprehensive given the chemical diversity of inhibitor molecules and the intricate nature of the surface–molecule interaction. In this work, we investigated two substituted benzothiazole derivatives as a case study to demonstrate how replaced chemical functionalities dominate the inhibition action and thereafter the stability of generated inhibitor film upon galvanised steel. By leveraging the particular mode of action, the designed inhibitor system has been proved effective for reinforcing the surface protection of post-corroded metal surface and shows promise for sustainable corrosion protection. This study is anticipated to provide new knowledge and insight for rational inhibitor engineering to realise tailored corrosion inhibition properties.

[a] *School of Engineering, RMIT University, Melbourne, VIC 3000, Australia.*
E-mail: qiushideng@hotmail.com, ivan.cole@rmit.edu.au
[b] *Catalan Institute of Nanoscience and Nanotechnology ICN2 (CSIC and BIST),*
Campus UAB, Bellaterra, 08193, Spain
[c] *BASF SE, Carl-Bosch-Srasse 38, Ludwigshafen am Rhein 67056, Germany*
[d] *BASF Coatings GmbH, Münster 48165, Germany. E-mail: patrick.keil@basf.com*
† Electronic supplementary information (ESI) available. See DOI: https://doi.org/
10.1039/d3me00153a

Introduction

Nowadays, increasing environmental awareness has propelled global endeavours towards reducing greenhouse-gas emission. As one of the pathways, effective and sustainable metal corrosion protection can alleviate the carbon footprint of the metal-producing industry when replacing corroded metal with the associated impact of additional CO_2

This journal is © The Royal Society of Chemistry and IChemE 2024

Mol. Syst. Des. Eng., 2024, **9**, 29–45 | 29

emission.[1] To achieve prominent corrosion inhibition, the use of corrosion inhibitors has been widely reported to mitigate effectively metal corrosion in corrosive environments.[2,3] Corrosion inhibitors within the organic regime are appreciably explored, which are commonly featured with (multi-)heterocycle(s) and/or functional groups, in which these electron-unsaturated fragments play a pivotal role in facilitating protective film formation upon the targeting metal.[4–6] However, challenges persist in high-efficiency inhibitor discovery due to the chemical diversity and structural complexity of the candidate pool. More so, the intricate role of replaced chemical functionalities regarding inhibition actions remains understudied, which is of essential importance to direct target-driven inhibitor discovery and molecular design.

Among diverse inhibitor molecules, studies on benzothiazole and its derivatives have never ceased on account of their pronounced corrosion inhibition performance. For instance, 2-mercaptobenzothiazole (2-MBT) is well known as an effective corrosion inhibitor for various metals such as copper and aluminium alloys.[7–10] The processed heteroatoms are potentially reactive sites enabling the metal–inhibitor interaction.[11] 2-MBT displays a tautomeric equilibrium and is presented in either thione ($>$C$=$S) or thiol (–SH) form. In addition to the conjugated heteroatoms, the attached thiol/thione as an additional reactive site further facilitates the 2-MBT molecule interaction with the targeting metal. Despite 2-MBT being one of the most studied corrosion inhibitors, debates remain in terms of its adsorption behaviour(s) and the subsequent film-forming mechanisms. Moreover, the nature of the formed inhibitive layer remains to be discussed, requiring in-depth investigation of inhibitor film growth kinetics, which is important information for further determining inhibitor analogues as well as structure-based molecular tailoring to enhance the inhibition effect.

In this regard, great contributions were made over the past years to unravel the underlying adsorption actions of 2-MBT on copper.[6,12] From a computational point of view, 2-MBT interacts strongly with different regions of the metal surface in that it forms covalent bonds on the oxide edge/surface via exocyclic S (S_{exo}) and endocyclic N (N_{endo}) and chemically bonds on metallic copper by S_{exo} and N_{endo} or both S atoms iso-energetically.[13] It has also been evidenced experimentally, in which different chemical states of S and N have been revealed for metallic copper and copper oxides.[14–16] Nonetheless, adsorption behaviour varies upon different metal substrates. A recent study examined the inhibition layer composition of 2-MBT upon zinc (Zn) after long-term immersion and proposed that 2-MBT forms an organometallic complex, i.e., Zn–(2-MBT) species, precipitating on zinc oxides and metallic Zn. The mixed compound of Zn, O and 2-MBT contributes to surface passivation.[17] Despite that, all these studies address the importance of (–SH/$>$C$=$S) of 2-MBT initiating the adsorption process.

The kinetics of the inhibitor film growth of 2-MBT have also attracted increasing attention to gain further mechanistic insights. Wu et al. studied the film evolution of 2-MBT over a pre-oxidised (2D) Cu surface and observed a thin inhibitor film formed by replacing the pristine oxide film, whilst in contrast, a thicker multi-layered inhibitor film was obtained at native copper oxides (3D).[15,18] Garg et al. fabricated an oxide-free Cu surface by cathodic polarisation and concluded that the advanced elimination of native oxides promotes a thicker and less defective protection layer, improving the barrier property against corrosion.[19] Although investigation has been progressively carried out on Cu, relevant studies on other metal surfaces, including Zn, are scarcely reported.

To further understand the inhibition actions of benzothiazoles to assist structural tailoring, this study investigated two substituted benzothiazoles, i.e., 2-MBT and 2-ABT, regarding their inhibition performance towards electrogalvanised steel (ZE) in an aqueous corrosive environment. The replacement of the attached chemical functionality helps clarify the role of –SH in the inhibition action with the metal. The corrosion inhibition effect was evaluated by means of potentiodynamic polarisation and electrochemical impedance spectroscopy. To determine the nature of inhibitor film growth, the interaction of the inhibitor molecule with the metal surface, dissolved metal ions and corrosion products was explored experimentally and theoretically using X-ray photoelectron spectroscopy, focused ion beam scanning electron microscopy, Raman spectroscopy and density functional theory simulation. Furthermore, it is important to investigate the adsorption stability of the formed protective film under corrosion conditions, i.e., to what extent the inhibitor film remains after time or under varying conditions. Thus, the inhibition performance upon polarised ZE surfaces was acquired. A simulated corrosion condition by superimposing overpotentials from 0 to +75 mV (vs. open circuit potential) was applied to replicate the resultant potential drop due to corrosion product formation or local protective film breakdown, and the subsequent protective inhibitor layer formation/breakdown kinetics was observed and discussed.

Experimental section

Sample preparation

The metal used in the study is electro-galvanised steel 75/75 (ZE), with a well-defined surface (90% of the orientation composed of {0001}), received from Chemetall, Frankfurt, Germany. The base substrate is cold-rolled steel, consisting of 98.5% Fe, 0.2% Si, 0.1% Al and 1.2% C by mass, which is used for automotive manufacturing. The galvanised surface is Zn with a purity of 99.99 wt%. Samples were cut into 2 cm × 6 cm and 1 cm × 1 cm sheets for electrochemical tests and surface analysis, respectively. Prior to each test, ZE samples were first immersed in a degreasing solution (buffered KOH, pH ~10.8) at 60 °C for 150 s, then rinsed with deionised (DI) water (Toc <2.6; resistivity >18 MΩ cm) and dried with a compressed nitrogen airflow. The prepared samples were stored in a desiccator for transferring purposes, and were

30 | Mol. Syst. Des. Eng., 2024, 9, 29–45

This journal is © The Royal Society of Chemistry and IChemE 2024

used within 1 h after the degreasing process. The chemical information of the investigated inhibitor candidates, *i.e.*, 2-aminobenzothiazole (2-ABT) and 2-mercaptobenzothiaozle (2-MBT), are given in Table 1. 0.1 M NaCl was prepared using DI water, to which the inhibitor candidate of desired concentration (0–1 mM) was added. The chosen concentration is considered aggressive for chloride-induced corrosion and representative to simulate a corrosion environment for galvanised steel.[20] A maximum concentration of 1 mM was applied for both inhibitor cases, given that this concentration level is close to the solubility limit of 2-MBT. Prior to each electrochemical test, the corrosion condition was unified by neutralising the solution to pH 7.0 (±0.5) using diluted HCl or NaOH.

Electrochemical measurements

A three-electrode conventional flat cell (K0235, AMETEK SI) was prepared, with a platinum mesh as counter electrode, a saturated Ag/AgCl electrode as reference electrode, and a ZE specimen assembled from the side delimited with a Teflon O-ring as working electrode. The surface area exposed to the corrosion medium was 1 cm^2, and a Luggin capillary was positioned at the proximity of the WE to minimise the IR drop of the solution. Electrochemical tests were performed using a Bio-logic VMP 300 potentiostat operated by Bio-lab software (version 11.57). Before each test, open circuit potential (OCP) was conducted for 90 min to ensure a quasi-stabilised corrosion system. All the tests were carried out at lab temperature (22 °C ± 1) and were done at least in triplicate to ensure repeatability.

Potentiodynamic polarisation scan (PDS) was performed at a scan rate of 1 mV s^{-1}, and a scan range from −0.05 V *vs.* OCP to 0.5 V *vs.* OCP and from 0.05 V *vs.* OCP to −0.5 V *vs.* OCP for the anodic and cathodic scans, respectively. The acquired PDS curves were compiled and analysed using the Tafel extrapolation method, where the electrochemical parameters such as corrosion potential (E_{corr}), corrosion current density (i_{corr}) and Tafel coefficients (β_a and β_c) were derived. Inhibition efficiency (IE) was calculated by eqn (1):

$$\text{IE } (\%) = \left(1 - \frac{i_{corr}^{inh}}{i_{corr}^0}\right) \times 100 \qquad (1)$$

where i_{corr}^0 and i_{corr}^{inh} are the corrosion current density of ZE specimens in NaCl solution without and with the addition of the inhibitor, respectively.

Electrochemical impedance spectroscopy (EIS) was conducted by superimposing a sinusoidal AC voltage of 10 mV$_{rms}$ with 10 points per decade measured at a frequency from 100 kHz to 10 mHz. Bio-logic software was used to fit the data obtained from the Nyquist plot. A combined Randomize and Simplex method with 50 000 iterations was used to produce the parameter regression calculation. IE was calculated using the following equation:

$$\text{IE } (\%) = \left(1 - \frac{R_{ct}^0}{R_{ct}^{inh}}\right) \times 100 \qquad (2)$$

where R_{ct}^0 and R_{ct}^{inh} are the charge-transfer resistance of ZE specimens in NaCl solution without and with the addition of the inhibitor, respectively.

Surface analysis

XPS analysis was performed using a Thermo K-alpha X-ray photoelectron spectrometer with a monochromatic Al Kα X-ray source (hv = 1486.6 eV). The X-ray source power was 90 W. The instrument baseline pressure was below 5×10^{-5} mbar, and the work function was calibrated referring to the Cu LMM auger peak. A co-axial flood gun was used for all the tested specimens to minimise the surface charging effect. The take-off angle was 90°, and the analysed area was 0.7 mm × 0.4 mm. The survey spectrum was measured using a pass energy of 160 eV and a step size of 1 eV. A high-resolution spectrum of the elements of interest was obtained from the same analysis area with a pass energy of 50 eV and a step size of 0.1 eV. Data analysis was conducted using CasaXPS (version 2.3.24 PR1.0, Casa Software Ltd). Shirley background subtraction and a generalised Lorentzian line shape LA (1.43, 243) were applied as provided by the software to all the peaks. The charge was corrected by setting the C–C bond of the C 1s peak to 285.0 eV.

The top and cross-sectional morphologies of the ZE specimen were examined using an FEI Scios Dual-beam FIB-SEM. FIB milling was performed under a 30 keV Ga ion beam. Prior to milling, a platinum strip was deposited upon the area of interest by a gas injection system. The milling process was initiated with a beam current of 0.3 mA to remove the bulk of the material, and progressively reduced current was introduced for the cross section to achieve a finer polished surface. Images were captured using an accelerating voltage of 20 keV and a current of 1.6 nA under high vacuum. The chemical composition was obtained using an inserted

Table 1 Chemical information of the candidate molecules in this study

Chemical	Structure	Supplier	Purity (%)	Molar mass (g mol^{-1})
2-Aminobenzothiaozle (2-ABT)		Tokyo Chemical Industry	98	150.20
2-Mercaptobenzothiazole (2-MBT)		Tokyo Chemical Industry	98	167.24

This journal is © The Royal Society of Chemistry and IChemE 2024

Mol. Syst. Des. Eng., 2024, **9**, 29–45 | 31

energy dispersive X-ray spectroscopy detector at an accelerating voltage of 5 keV.

A Bruker dimension icon atomic force microscope (AFM) was employed to acquire surface topography. Images (256 × 256 resolution) were recorded under a scan rate of 1 Hz operated in ScanAsyst air mode. The maximum force applied was 42 nN, and the scan area was 20 μm × 20 μm. The height profile of the investigated surface was selected for further data analysis using Nanoscope analysis software (version 1.9).

Surface profile measurements were conducted using a Contour GT-K Bruker nano 3D optical profilometer operated by SurfVision software. Data analysis was carried out using Vision64 software (version 5.70).

Raman spectroscopy was carried out using a Raman station 400 spectrometer with a laser excitation wavelength of 785 nm. The Raman spectrum was obtained at a resolution of 4 cm^{-1} in a range from 150 to 1800 cm^{-1}. The integration time was 5 s, and the integration number was 15.

Computational methods

Density functional theory (DFT) simulations were performed using the SIESTA package, a DFT method for *ab initio* electronic structure calculations, which uses a basis set of strictly localised atomic orbitals and norm-conserving pseudopotentials.[21–23] This approach allows us to model systems of dozens to hundreds of atoms with a modest cost and high accuracy. The Perdew–Burke–Ernzerhof (PBE) method was chosen to treat the electron exchange and correlation terms, within the generalized gradient approximation (GGA).[24] The conjugated gradient method was employed for structural optimization and electronic structure calculations, where atomic forces below 0.01 eV Å^{-1} were considered converged. An electronic temperature of 25 meV was chosen to smear the electronic occupations with a Fermi–Dirac distribution function. For all the calculations, a tolerance of 10^{-4} was set up for the density matrix as convergence criterion for the SCF cycle.

Bulk zinc was first studied to obtain the theoretical equilibrium lattice parameters $\vec{a} = \vec{b} = 2.70$ Å, $\vec{c} = 4.88$ Å ($\alpha = \beta = 90°$, $\gamma = 120°$), which are in good agreement with the reported ones in Materials Project database.[25] A mesh cut-off of 600 Ry for the real space integrals and a Monkhorst–Pack k-grid of 30 × 30 × 15 were used for the bulk calculations. The ZE surface was modelled using an orthorhombic 6-layered (4 × 4) Zn{0001} slab, which is the predominant grain orientation in our samples, with the lattice vectors $\vec{a} = 10.800$, $\vec{b} = 9.353$ Å, $\vec{c} = 42.200$ Å, built from an optimized Zn primitive cell. A vacuum layer of 20 Å in the z direction was considered within the slab to prevent interactions among periodic images. During the optimization of the Zn{0001} slab, the two outermost layers were allowed to relax while the remaining four bottom ones were kept frozen. The Brillouin zone of the surface cases was sampled using a 6 × 6 × 1 Monkhorst–Pack k-grid, and the real space integrals were done with a mesh cut-off of 400 Ry.

For the isolated molecules (2-MBT and 2-ABT), structural optimization was performed for each of them using a cubic cell with a lattice constant of 30 Å to avoid interaction between periodic images. In this case, the Γ-point was used to sample the Brillouin zone, and a mesh cut-off of 400 Ry was chosen for the real space integrals.

Double-ζ basis sets with polarization (DZP) orbitals were used to describe the valence electrons of all systems. The basis sets for the different chemical species were optimized variationally to obtain the best basis set (lowest total energy) in terms of the cut-off radius (r_c), soft confinement potential, ionic charge, and split norm parameters.[26] In the case of Zn surface, the inner atoms (second to fifth layers) were simulated using the standard DZP scheme of SIESTA with an energy shift parameter of 0.0001 Ry to define the r_c, while the surface ones (first and sixth layer) with an extra shell of diffuse functions with s symmetry and confined within a cut-off radius. These extra orbitals in the surface atoms describe better the long decay of the wave functions into vacuum.[27] In this case, the selected diffuse orbital was the 5s orbital with an optimized cut-off radius of 6.8 a.u.

Troullier–Martins pseudopotentials in the psf format were used for the chemical species in the molecules, and norm-conserving pseudopotentials in the PSML format for Zn. During the adsorption of the molecules onto the surface, van der Waals interactions were described using the D2 Grimme's parametrization, which does not pose an additional computational cost over that of the PBE functional. Dipole corrections were applied to avoid the effect of net dipole of the asymmetric slabs.[28–31]

The molecular adsorption is considered according to the following equation:

$$n\text{MBT/ABT} + \text{Zn}\{0001\}_{\text{surface}} \rightarrow n\text{MBT/ABT} - \text{Zn}\{0001\}_{\text{surface}} \quad (3)$$
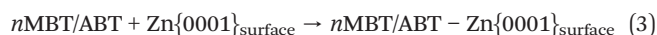
where n is the number of molecules adsorbed, MBT/ABT is the isolated inhibitor molecule, Zn{0001}$_{\text{surface}}$ is the Zn surface, and MBT/ABT $-$ Zn{0001}$_{\text{surface}}$ is the inhibitor adsorbed system. The adsorption energy (E_{ads}) is calculated as follows:

$$E_{\text{ads}} = (E_{n\text{MBT/ABT}-\text{Zn}\{0001\}} - nE_{\text{MBT/ABT}} - E_{\text{Zn}\{0001\}}/A) \quad (4)$$

where $E_{\text{MBT/ABT}-\text{Zn}\{0001\}}$ is the energy of inhibitor bonded to the Zn{0001} surface, $E_{\text{MBT(ABT)}}$ is the energy of the isolated molecule, $E_{\text{Zn}\{0001\}}$ is the energy of the Zn{0001} surface, and A is the area of the surface (nm^2). From this definition, the lower the value (more negative) of E_{ads}, the higher the stability of the adsorption.

The inhibitor adsorption was evaluated under two different concentrations: (1) low – one molecule per cell ≈ 0.98 molecules per nm^2 and (2) high concentration – three molecules per cell ≈ 2.96 molecules per nm^2 which correspond to a self-assembled monolayer (SAM) case.

32 | *Mol. Syst. Des. Eng.*, 2024, **9**, 29–45

This journal is © The Royal Society of Chemistry and IChemE 2024

Results and discussion

Corrosion inhibition effect determined by PDS

PDS was performed to explore the corrosion kinetics and quantify the inhibition effect of inhibitor candidates (Fig. 1a and b). The addition of either candidate decreases both anodic and cathodic current densities compared to the blank (inhibitor-free case). Moreover, a concentration-dependent inhibition effect was observed for both 2-ABT and 2-MBT, where at 1 mM an enhanced corrosion mitigation was discerned at both branches. The corrosion potential (E_{corr}) of 2-ABT is more increased at increased concentrations, signifying a more anodic inhibition characteristic preventing metal dissolution. This is also indicated by the "shoulder" feature appearing at approx. −880 mV$_{Ag/AgCl}$ at 1 mM, implying a more passive nature endowed to ZE at high 2-ABT concentration. Similar features were also obtained at the anodic branches in the case of 2-MBT. Nonetheless, more mixed-type inhibitive activity of 2-MBT is indicated at 1 mM with E_{corr} close to that of the blank. This could be attributed to the fact that 2-MBT interacts preferentially with anodic sites, while at high concentration an increasing surface coverage towards both anodic and cathodic sites of ZE is obtained.

Table 2 summarises the electrochemical parameters derived by the Tafel extrapolation method and calculated IE values using eqn (1).[32] The standard deviation (Dev.) is also presented by averaging the IE values derived for triplicate PDS measurements. It is suggested by Tafel slopes (β_a and β_c) that the presence of either inhibitor candidate suppresses the corrosion kinetics of both corrosion reactions, which agrees with the PDS curve interpretation. In addition, the i_{corr} values reduce with increasing concentrations. In general, both inhibitor candidates render improved corrosion inhibition at high concentration, in which 2-MBT outperforms with an IE value of 81% at 1 mM.

Interfacial states of inhibited ZE surface

EIS was further conducted to examine the metal–solution interface in the presence of inhibitors. Fig. 2 shows the representative EIS Nyquist plots obtained after 90 min immersion of a ZE specimen in 0.1 M NaCl with inhibitor candidate at different concentrations (0–1 mM). In the inhibitor-free solution, the Nyquist diagram demonstrates two depressed semicircles indicating two relaxation processes, where at low frequency range the capacitive loop is
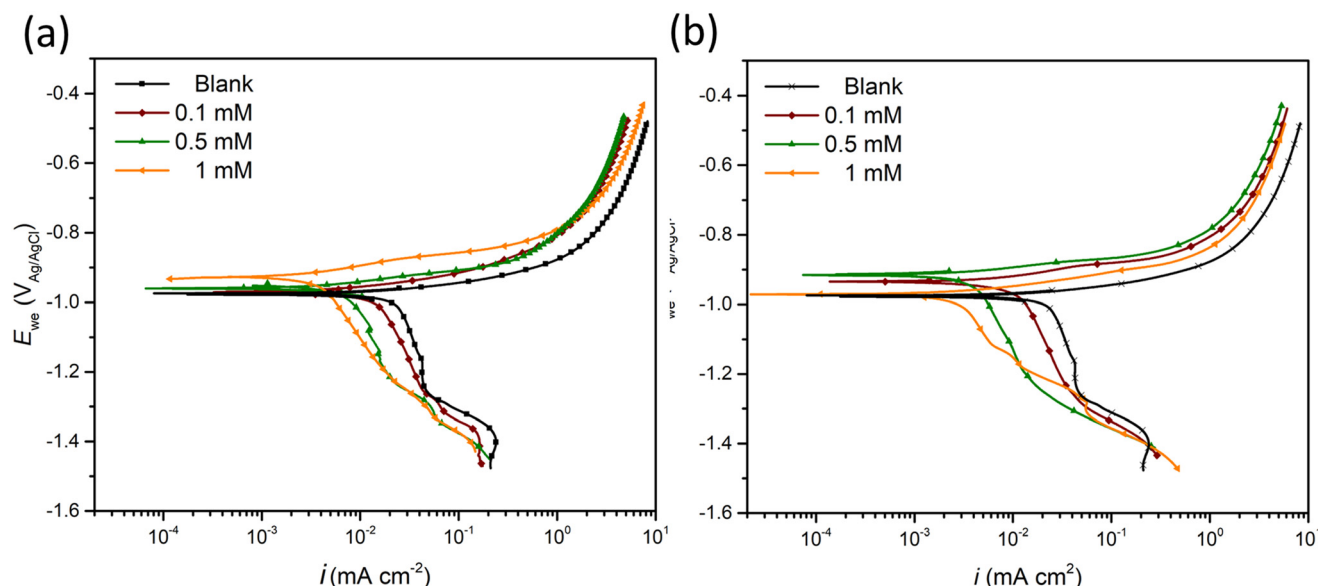
Fig. 1 PDS curves of ZE specimen after 90 min immersion in NaCl solution in the presence of (a) 2-ABT and (b) 2-MBT at different concentrations (0–1 mM).

Table 2 Electrochemical parameters derived from PDS curves and calculated IE values of ZE in 0.1 M NaCl in the presence of inhibitor candidate at different concentrations

	Concentration (mM)	E_{corr} (V$_{Ag/AgCl}$)	β_a (mV dec^{-1})	β_c (mV dec^{-1})	i_{corr} (μA cm^{-2})	IE (%)	Dev. (%)
Blank	—	−0.976	21.9	44.7	6.01	—	—
2-ABT	0.1	−0.967	31.1	55.8	3.22	46	21
	0.5	−0.951	30.8	73.3	1.61	73	12
	1	−0.934	31.2	78.2	1.36	77	6
2-MBT	0.1	−0.932	24.6	50.7	2.66	56	15
	0.5	−0.916	24.4	74.7	1.41	77	5
	1	−0.975	26.4	77.6	1.13	81	4

This journal is © The Royal Society of Chemistry and IChemE 2024

Mol. Syst. Des. Eng., 2024, **9**, 29–45 | 33
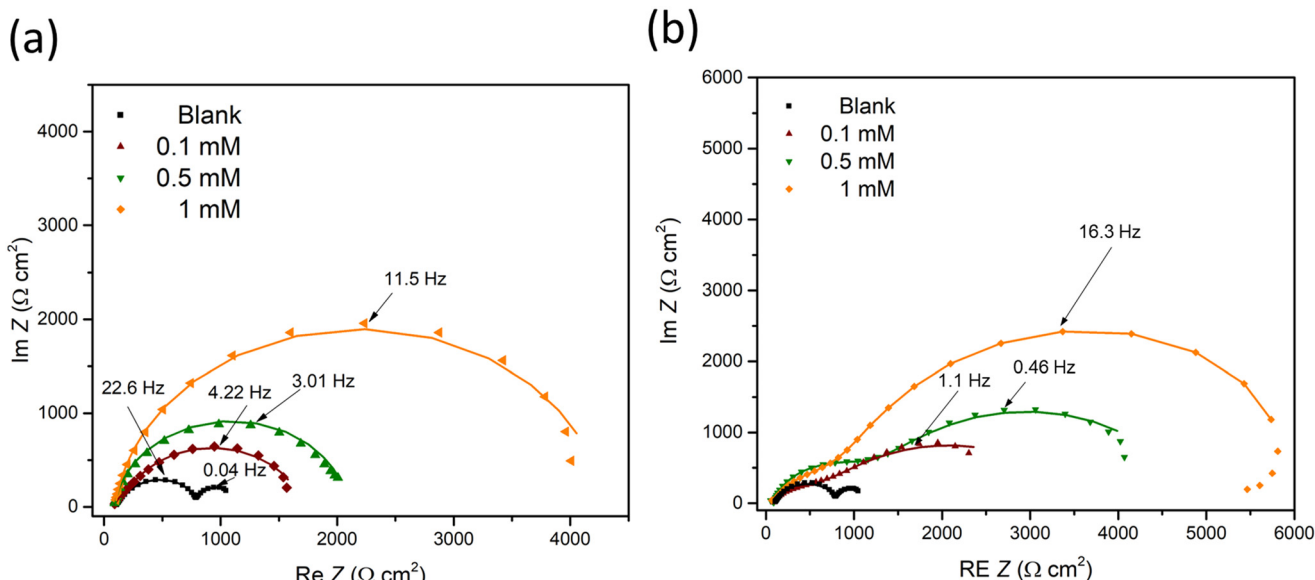
Fig. 2 EIS diagrams of ZE specimen after 90 min immersion in NaCl solution with inhibitor at different concentrations (0–1 mM). (a) 2-ABT; (b) 2-MBT.

ascribed to the charge transfer process of ZE and at middle to high frequency range the semicircle can be related to the capacitive response of zinc oxides/corrosion products.[33] The small impedance arc also reflects mild corrosion resistance of ZE in saline solution.

The addition of either inhibitor candidate increases the impedance modulus, presumably as a result of the inhibition action of the added molecule. With increasing inhibitor concentration, more enlarged capacitance semicircles were acquired, implying the increased surface coverage of inhibitor molecules *via* the adsorption process. Note that only one capacitive response was determined in the case of 2-ABT. For 2-MBT, in contrast, two relaxation processes remain where the impedance modulus at low to middle frequency is increased to a greater extent, indicating a different interfacial condition compared to that of 2-ABT.[34]

Based on the determined interfacial behaviours, two equivalent electric circuit (EEC) models were employed to fit the Nyquist plot, as shown in Fig. 3. R_s is the solution resistance, R_{ct} and R_f are the resistance of the electric double layer and product/inhibitor film, respectively. Constant phase elements were used to model the non-ideal

capacitive response at the interface, which could be expressed as follows:

$$Z_{CPE} = Y_0^{-1}(j \cdot 2\pi f)^{-n} \tag{5}$$

$$n = 1/(D - 1) \tag{6}$$

where Y_0 is the admittance of the CPE. f and j are the frequency and the imaginary unit ($j^2 = -1$), respectively. n is the empirical exponent ($0 \leq n \leq 1$). D is the fractural dimension of the surface ($2 \leq D \leq 3$), in which for a uniform interfacial condition resembling a nearly parallel-plate capacitor ($D \simeq 2$) the value of n is close to 1.

The actual capacitance of the double layer (C_{dl}) can be derived from the CPE:

$$C_{dl} = Y_0(2\pi f_{max})^{n-1} \tag{7}$$

where f_{max} is the frequency with the maximum impedance value of the imaginary part in the Nyquist plot.

The determined EIS parameters are recorded in Table 3, and the IE values were calculated. The values of R_{ct} increase
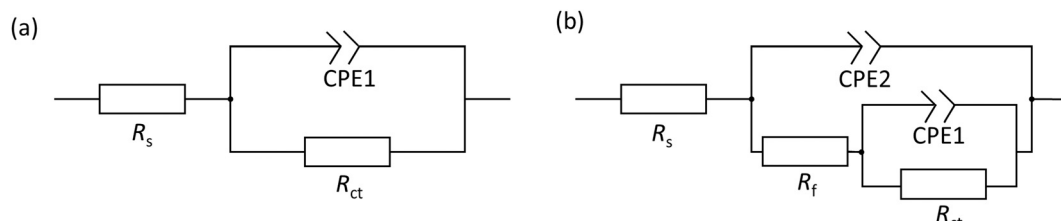

Fig. 3 EEC models used for EIS fitting. R_s, R_f and R_{ct} are the resistance of the solution, inhibitor/product film, and charge transfer, respectively. (a) CPE1 is the constant phase element simulating the double layer capacitance, and (b) CPE2 represents the response of inhibitor film/corrosion product film.

34 | *Mol. Syst. Des. Eng.*, 2024, **9**, 29–45

This journal is © The Royal Society of Chemistry and IChemE 2024

Table 3 Electrochemical parameters obtained from EIS of ZE after 90 min immersion in 0.1 M NaCl with the addition of inhibitor candidate at different concentrations (0–1 mM)

Sample	Conc. (mM)	R_s (Ω cm^{-2})	CPE1 Y_{dl} (mΩ^{-1} s^n cm^{-2})	n_1	C_{dl} (μF cm^{-2})	R_{ct} (Ω cm^{-2})	CPE2 Y_f ($\mu\Omega^{-1}$ s^n cm^{-2})	n_2	R_f (Ω cm^{-2})	$\chi^2/|Z|$ (10^{-3})	IE (%)
Blank	—	82	43.2	0.82	55.4	723	9.4	0.92	387	8.54	—
2-ABT	0.1	81	35.3	0.95	29.9	1573				8.83	54
	0.5	83	23.5	0.92	18.1	1990				3.85	64
	1	84	4.33	0.93	3.3	4023				3.91	82
2-MBT	0.1	79	47.4	0.69	3.9	2870	3.8	0.71	679	7.15	75
	0.5	86	8.7	0.86	2.5	3487	3.4	0.75	1294	1.86	79
	1	73	7.5	0.68	2.3	5127	2.3	0.99	1771	4.93	86

with inhibitor concentration possibly due to the coverage effect at the interface mitigating corrosion activity. Both inhibitor molecules interfere with the charge-transfer process, giving rise to higher R_{ct} values than that of the blank. In both inhibitor cases, the CPE unit was implemented, in which the fit parameter, the exponent n, varies from 0.68 to 1 (D between 2 and 2.5). This is often related to the frequency dispersion by surface roughening and/or inhomogeneous reaction rate by the adsorption of inhibitor molecule.[33,35] Nonetheless, the exponent of 2-MBT shows a less consistent condition with much reduced n values, likely associated with the inhomogeneous distribution of inhibitor layer upon the metal. This is also evidenced by the AFM and SEM results of inhibited surface morphology (discussed in the following section). In contrast, the 2-ABT interface is more consistent, with n values close to 1, which can be related to more general surface coverage of the presented inhibitor film. Consequently, the determination of layer capacitance based on Y becomes less quantitative taking into account the non-ideal capacitive behaviour due to the rough/fractal interfacial condition. Nonetheless, the equivalent capacitance value can be derived for comparison purposes through eqn (7), where in both cases the values of C_{dl} decrease as compared to that of the inhibitor-free system. Based on the Helmholtz model, capacitance is a function of the film thickness (d), the permittivity of vacuum (ε_0, 8.85 × 10^{-12} F m^{-1}), relative dielectric constant (ε_r) and effective surface area (A, 1 cm^{-2}) of the double layer, shown in eqn (8).

$$C = \frac{\varepsilon_0 \varepsilon_r}{d} \cdot A \tag{8}$$

The decrease of C_{dl} can be associated with the water displacement by the adsorption inhibitor molecules, reducing the exposed metal area against the corrosive medium. A lower C_{dl} value at increased inhibitor concentration is therefore assigned to greater surface coverage density of inhibitor films, leading to enhanced corrosion inhibition. This is also in line with the inhibition efficacy observed for both inhibitor cases. In addition, the inhibitor film thickness can be estimated from Y_f using eqn (7) and (8). A previous study has reported an ε_r value of 6.29 for 2-MBT film adsorbed onto the Cu surface.[36] Whilst the actual ε_r varies associated with the homogeneity of the

surface and the nature of the film, the same order of magnitude of film thickness would be expected. Thus, the thickness of 2-MBT film formed upon ZE is approx. 0.13 μm, 0.15 μm, and 0.22 μm at 0.1 mM, 0.5 mM and 1 mM, respectively, which indicates the film growth at increasing concentration endowing improved surface protection.

Inhibited surface characterisation

To further characterise the inhibited ZE surface, SEM imaging was conducted on ZE specimens after 90 min immersion in both uninhibited and inhibited NaCl solutions (Fig. 4). As compared to the ZE fresh surface, the presence of corrosion products was observed for ZE after immersion in inhibitor-free solution. The introduction of 2-ABT at a concentration of 1 mM almost preserves the pristine morphology of the ZE substrate, signifying the sufficient inhibition effect of retarding ZE corrosion. Whist EDX scan recorded certain chemical compositions of the inhibitor (Fig. S1†), the presented film of 2-ABT can be barely observed within micro-scale. A previous study on the inhibition performance of 2-amino-4-methylthiazole (2AT-Me) has reported similar surface morphology of the inhibited ZE surface, which is attributed to the chemisorbed nature of the thin inhibitor layer.[20] For 2-MBT, surface morphology differs in that micro-sized particles are discerned upon the ZE surface. The chemical composition revealed by EDX (Fig. S2†) indicates that these particles are facilitated by the presence of the 2-MBT molecules.

Furthermore, inhibited ZE surfaces were characterised by AFM and OP as shown in Fig. 4. Here, to better reveal the underlying corrosion activity and product formation, ZE specimens were polished (down to 0.6 μm) to ensure consistent surface condition before each measurement. It becomes evident upon polishing the ZE specimens that localised corrosion takes place after immersion in plain NaCl solution. Corrosion products with irregular shape were also captured in sweeping AFM results. While similar AFM topography was displayed of 2-MBT, it is noted from the correspondent OP result in a greater scale that more densified island-shaped products on a microscale are precipitated in the presence of 2-MBT molecules, which is in line with the previous SEM and EIS analyses. This is in

This journal is © The Royal Society of Chemistry and IChemE 2024

Mol. Syst. Des. Eng., 2024, **9**, 29–45 | 35
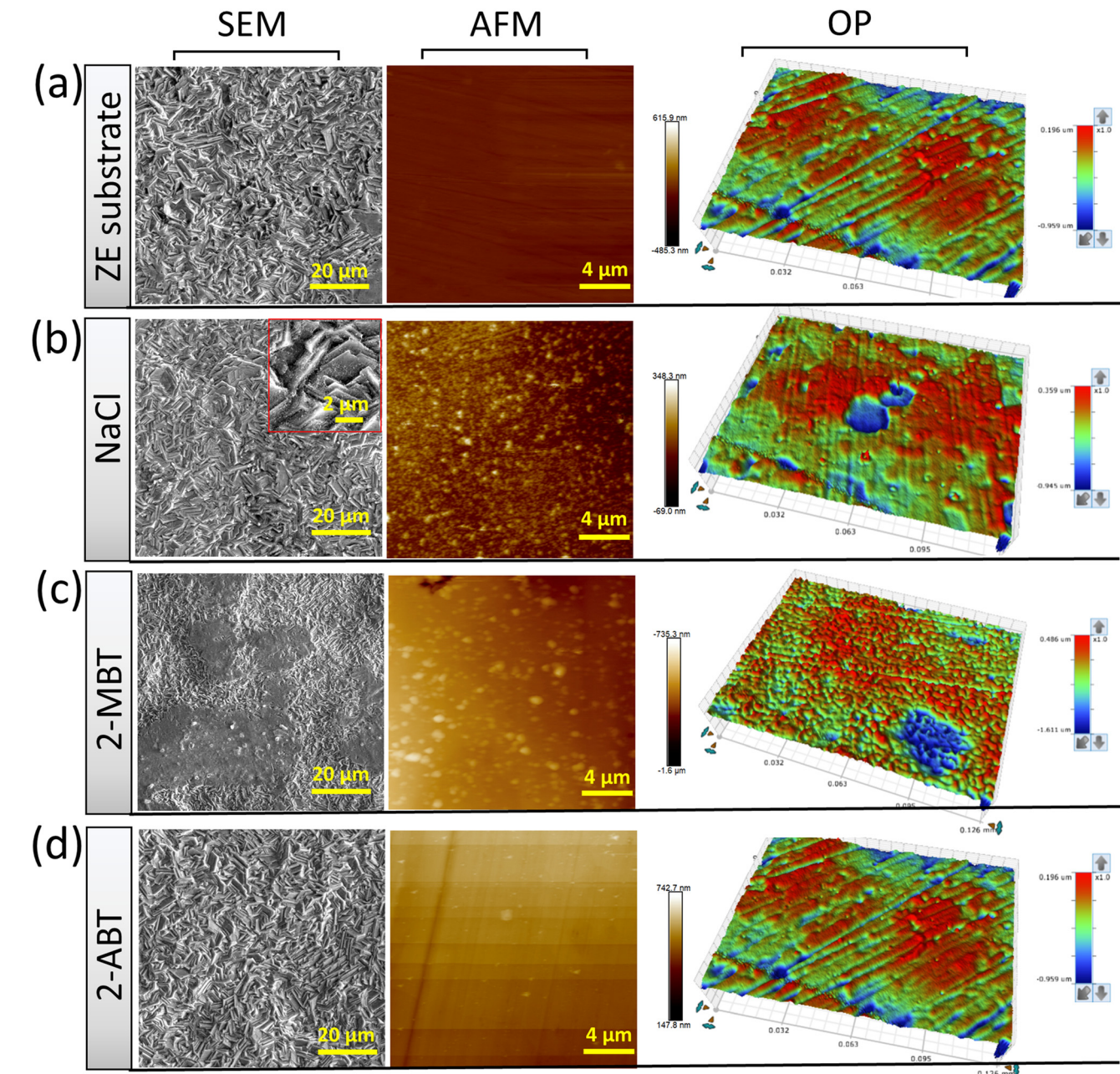
Fig. 4 Surface morphology at different resolutions of ZE specimens under different corrosive conditions. (a) ZE substrate, (b) ZE after 90 min immersion in 0.1 M NaCl, (c) and (d) ZE specimens after 90 min immersion in 0.1 M NaCl in the presence of 1 mM 2-MBT and 2-ABT, respectively.

contrast to the ZE specimen after being treated with 2-ABT, where both AFM and OP results show insignificant changes of the surface, presumably due to the formation of a more homogenous inhibitor film.

Adsorption mechanism

XPS analysis was further performed to explore the adsorption mechanism. Previous studies on thiazole derivatives suggested that the heteroatoms are key to facilitating metal–molecule interaction due to their electron-unsaturated nature.[37] Therefore, the chemical environments of S 2p and

N 1s were analysed as important fingerprints to determine the binding states of inhibitor molecules on the metal. Fig. 5 and 6 exhibit the high-resolution S 2p and N 1s spectra of the chemical powder (reference) and inhibited ZE surface for the case of 2-ABT and 2-MBT, respectively. To determine the underlying interaction of the candidate inhibitor with the metal ions in solution, mixtures of inhibitor molecule and $ZnCl_2$ (Inhn-Me) at a molar ratio of 1 : 2 were also prepared, in which any precipitated solids were then segregated for XPS analysis. The corresponding spectra were also recorded.

For S 2p spectra of both cases, the fitting was conducted using spin–orbit doublets S $2p_{1/2}$ and S $2p_{3/2}$ with a
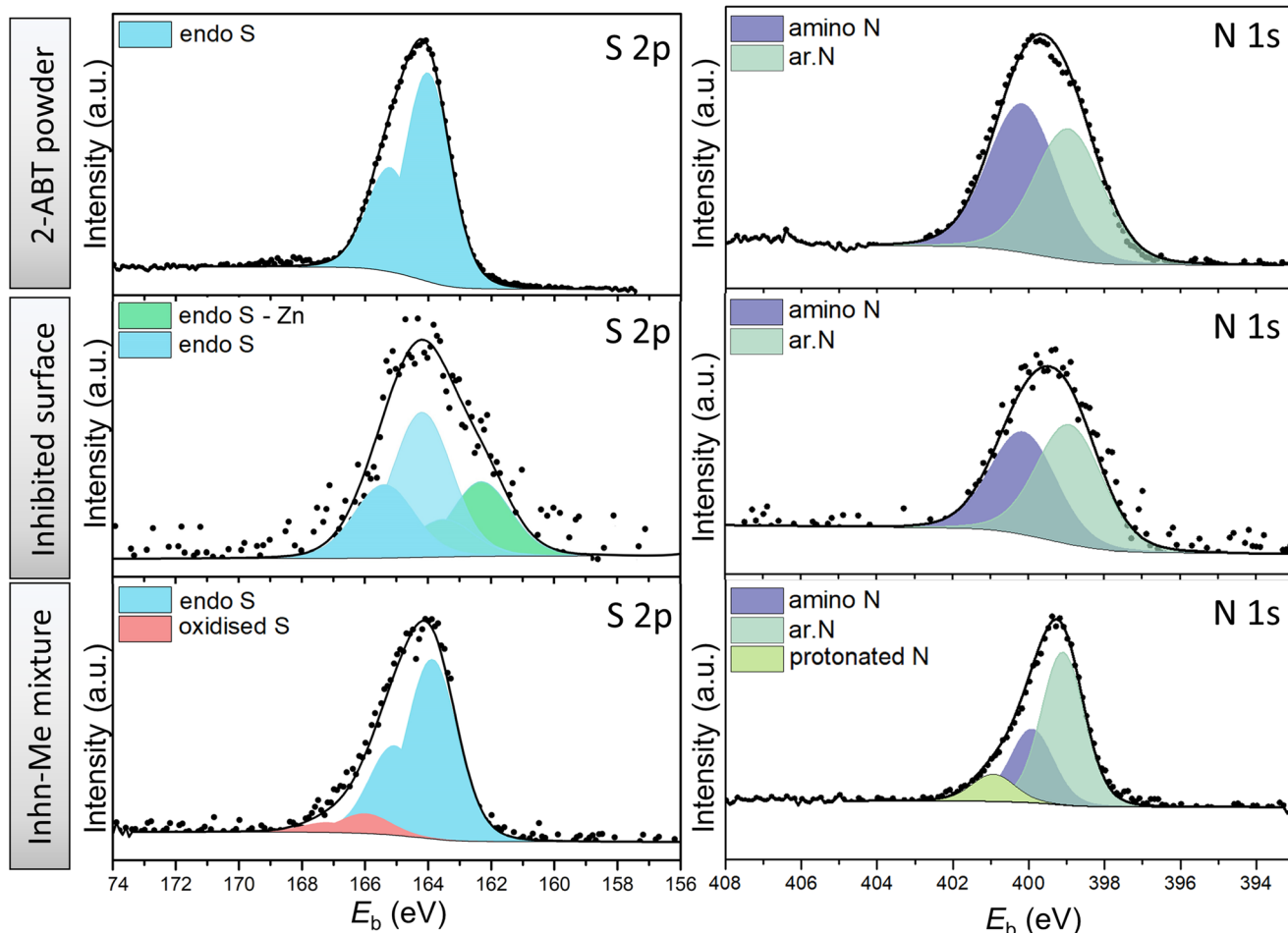
Fig. 5 High-resolution XPS spectra of S 2p and N 1s of 2-ABT powder (reference), ZE surface treated with 2-ABT and precipitates of inhibitor solution mixed with ZnCl$_2$.

branching ratio of 0.5 and spin–orbit splitting of 1.2 eV. For 2-ABT powder, only one S state was resolved, assigned to the endocyclic (endo) S (164.1 eV) of the aromatic (ar.) ring.[14] Identical S 2p binding energy was obtained for the separated solid of the Inhn-Me mixture of 2-ABT, except for a small amount of S at higher binding energy (166.0 eV) obtained possibly due to S oxidation (SO$_x$) by the evaporation procedure of the remaining solution.[38] This suggests that 2-ABT retains its molecular form, unable to coordinate with the added Zn^{2+}. In contrast, an additional chemical environment at lower binding energy, *i.e.*, 161.9 eV, was resolved for the inhibited ZE surface (Fig. 5). The binding energy shift can be assigned to a chemisorbed 2-ABT molecule with electron-rich S resulting from the electron transfer process.[39] This also agrees with previous studies on 2-ABT regarding the adsorption behaviour towards Cu, where chemisorbed state *via* S heteroatom was reported.[15]

On the other hand, the chemical environment of N 1s of the ZE surface inhibited by 2-ABT remains identical with its chemical powder. Peak components centred at 399.0 eV (±0.1) and 400.0 eV (±0.1) were resolved to correlate with the ar. N and amino N, respectively.[10,40] A branching ratio of 1.12

is nearly identical to the N stoichiometry of the 2-ABT molecule, suggesting that neither of the N atoms forms a chemical bond with the metal surface. Indeed, the amino group of 2-ABT possesses a pK_α value in the range of 10–11, which indicates that the amino N coordinates with metal ions only under an alkaline environment.[3] Correspondingly, in the case of the Inhn-Me mixture, an additional N environment at a binding energy of 400.8 eV was obtained, mostly associated with the protonated 2-ABT molecule.[10]

The S 2p spectrum of 2-MBT powder was decomposed with two main components, *i.e.*, endocyclic/ar. S (164.3 eV) and exocyclic S (162.2 eV).[18,41] A small amount of oxidised S was also observed. Note that 2-MBT can exist in both thione and thiol forms, resulting in two different N environments, *i.e.*, imine N (C=N) and amine N (C–N–H) (Fig. S3†).[42] Previous studies suggest that the thione form of 2-MBT predominates in the solid state.[43] A similar finding has been observed in our case, as the peak component of amine/ protonated N (400.8 eV) was decomposed, which can be ascribed to the presence of 2-MBT in the thione form.

Nevertheless, the S 2p environments of both inhibited ZE surface and the segregated solids show a higher binding

This journal is © The Royal Society of Chemistry and IChemE 2024

Mol. Syst. Des. Eng., 2024, **9**, 29–45 | **37**
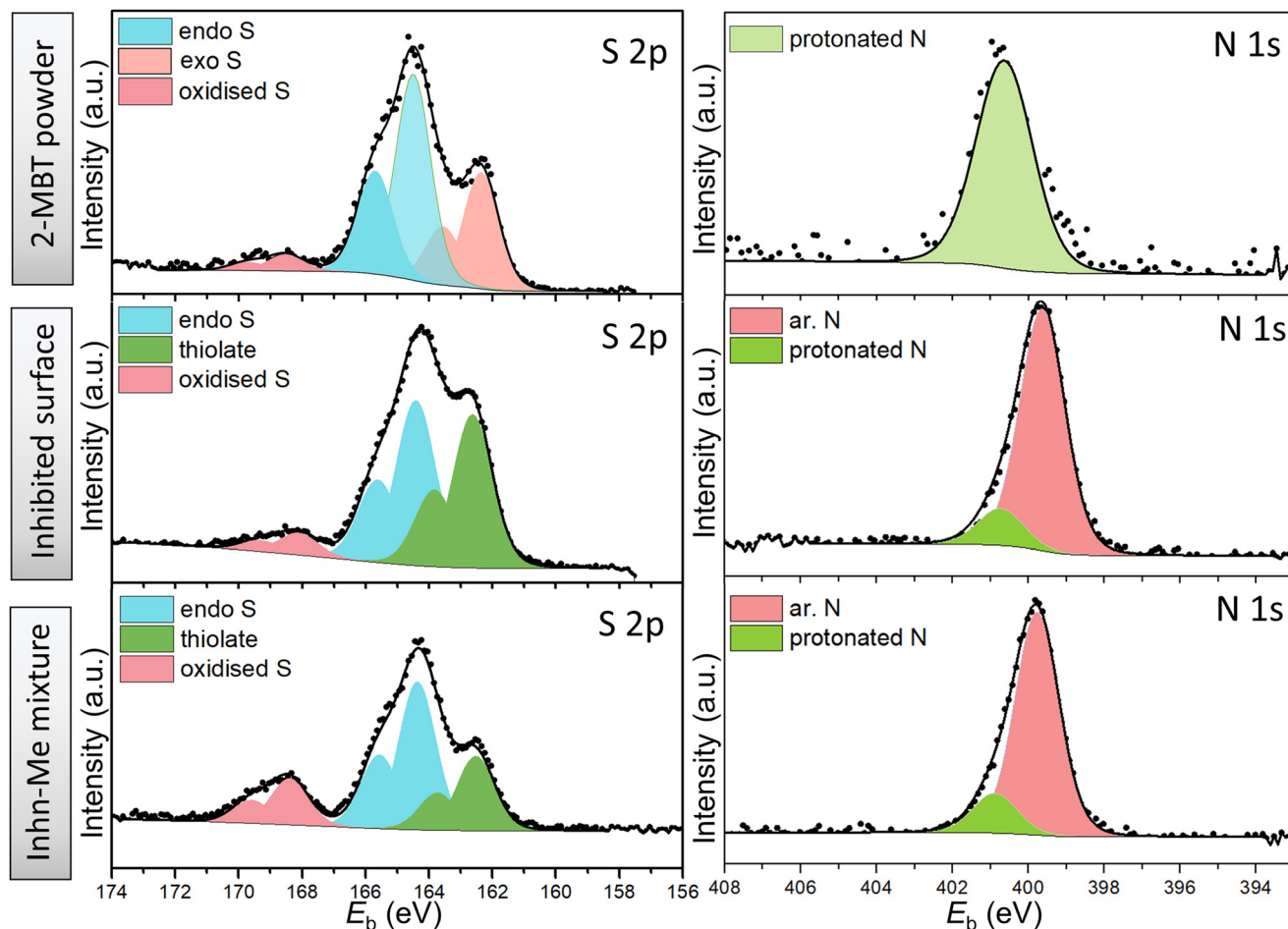
Fig. 6 High-resolution XPS spectra of S 2p and N 1s of 2-MBT powder (reference), ZE surface treated with 2-MBT and precipitates of inhibitor solution mixed with ZnCl$_2$.

energy shift of exocyclic S (162.6 eV, *i.e.*, +0.4 eV). This corresponds to the presence of thiolate presumably due to the thiol/thione group interacting with Zn cation.[44] In addition, it is noted that the concentration of protonated N of the N 1s spectrum reduces significantly in both cases, suggesting that the thiol form of 2-MBT predominates when interacting with the metal in solution. Noted also is that one main peak positioned at 399.7 eV was obtained, where two possibilities may exist to explain the shift of +0.7 eV from the binding energy of C=N (399.0 eV). First, this relates to the underlying chemical binding between the ar. N *via* the free electron pair and the vacant outer orbital of Zn^{2+}. It has been reported that the metal–inhibitor coordination is more energetically favoured by chelation, that is, by both thiol and adjacent ar. N of 2-MBT.[45] Alternatively, as S is bound to Zn, the electronic density of other atoms in the molecule may change, leading to the binding energy shift of ar. N.[15] Nonetheless, it has to be mentioned that the chemical compositions of S and N of the inhibited surface are identical with those of the segregated precipitates from the 2-MBT/ZnCl$_2$ solution mixture. This suggests that 2-MBT is able to form complexes with released Zn^{2+} *via* the thiol group and ar. N, which is presumed to initiate the subsequent product

precipitation upon the ZE surface. Thereby, this adsorption action leads to inhomogeneous inhibition layer formation, as evidenced by both SEM and OP results.

Further investigation on the molecule–surface interaction was carried out from a modelling perspective. To simplify the adsorption model of 2-MBT on the surface, the thione form of 2-MBT was used for our calculations. This approach circumvents the need to model a charged chemical compound (thiolate), which can introduce complications
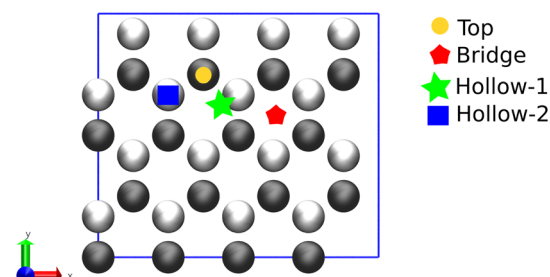
Fig. 7 Different adsorption sites at the Zn-{0001} plane. Top (yellow circle), bridge (red pentagon), hollow-1 (green star), and hollow-2 (blue square) represent the different possible adsorption sites. Gray-colored spheres: Zn surface; degraded color spheres: Zn under surface.

38 | *Mol. Syst. Des. Eng.*, 2024, **9**, 29–45

This journal is © The Royal Society of Chemistry and IChemE 2024

when employing periodic boundary methods such as those used in DFT. Due to its higher stability compared to the thiol form, the thione form was considered in our analysis as it is reported to have minimal influence on the adsorption process. Nonetheless, it has been revealed that both tautomeric cases exhibit very similar final adsorption configurations, with the only notable difference being the higher E_{ads} values observed in the thiolate counterparts.[6] Fig. 7 depicts the different possible adsorption sites presented on the topmost surface plane considered in the simulation for the vertical adsorption of the inhibitor, where either the S atom or the NH_2 group is pointing out to the Zn surface.

At low concentration of 2-MBT (single molecule case), four adsorption modes were determined as the most stable configurations towards the metal surface. The adsorption geometries were denoted using the atom(s) linked to the Zn surface, i.e., (S)-Zn (one S atom attached to the surface in a hollow site), (S,S)-Zn (two S atoms linked to the surface), (S, NH)-Zn (one S atom and NH directed to the surface), and a tilted (nearly parallel) configuration. Fig. 8 shows the most stable configuration of 2-MBT at low concentration. The molecule is nearly parallel towards the surface with an adsorption energy of -36.381 kcal mol^{-1} nm^{-2}. In addition, it is discerned that in the configurations of (S,S)-Zn and (S,NH)-Zn, the interacting Zn atom is pulled out of the plane with a distance of approx. 0.33 and 0.39 Å, respectively. This can be related to the strong interaction between these chemical functionalities (particularly exocyclic S) and the metal surface. Nonetheless, when the exocyclic S is directed solely towards Zn, the obtained E_{ads} is the lowest, which indicates the collaborative effort induced by ar. N to strengthen the surface–molecule interaction. The adsorption stability for 2-ABT at low concentration is similar to that of 2-MBT (Fig. S4 and S6†), with the E_{ads} ranking as follows: parallel > (N, NH_2)-Zn ≈ (S,NH_2)-Zn > (NH_2)-Zn.

At high coverage of 2-MBT, the molecules stabilised in a perpendicular orientation towards the surface, with (S,NH)-Zn and (S,S)-Zn the most stable geometries (Fig. 8). In contrast to the single molecule, an increased E_{ads} was observed in the system. The E_{ads} value in the case of (S, NH)-Zn and (S,S)-Zn increases by -5.232 kcal mol^{-1} per molecule and -6.724 kcal mol^{-1} per molecule (Table S1†), respectively. The enhanced adsorption stability could be related to the augmented π–π interaction in the system. Similar to the isolated molecule case, the Zn atom from the surface is pulled out 0.48 Å by the exocyclic S. In the case of 2-ABT, two adsorption states were determined, i.e., (N, NH)-Zn and (S,NH)-Zn, with E_{ads} values at a similar level (Fig. S5 and S6†). As compared to the single molecule case, the molecule at full coverage gains an adsorption energy of -6.440 kcal mol^{-1} per molecule and -9.102 kcal mol^{-1} per molecule, respectively, due to the aforementioned π–π stacking stabilising the surface interaction which favours the adsorption process. Nonetheless, the repulsion between molecules in the assembled inhibitor layer leads to a more disorganized structure, with a significant role played by H atoms in the NH_2 group. Overall, it is evident that the presence of the thiol group of benzothiazole affords greater adsorption strength as compared to the amino group by acting as a reactive site. Additionally, the predominant adsorption geometry in a tilted form at a high concentration further enhances the molecular binding through these anchoring parts (Fig. 9).
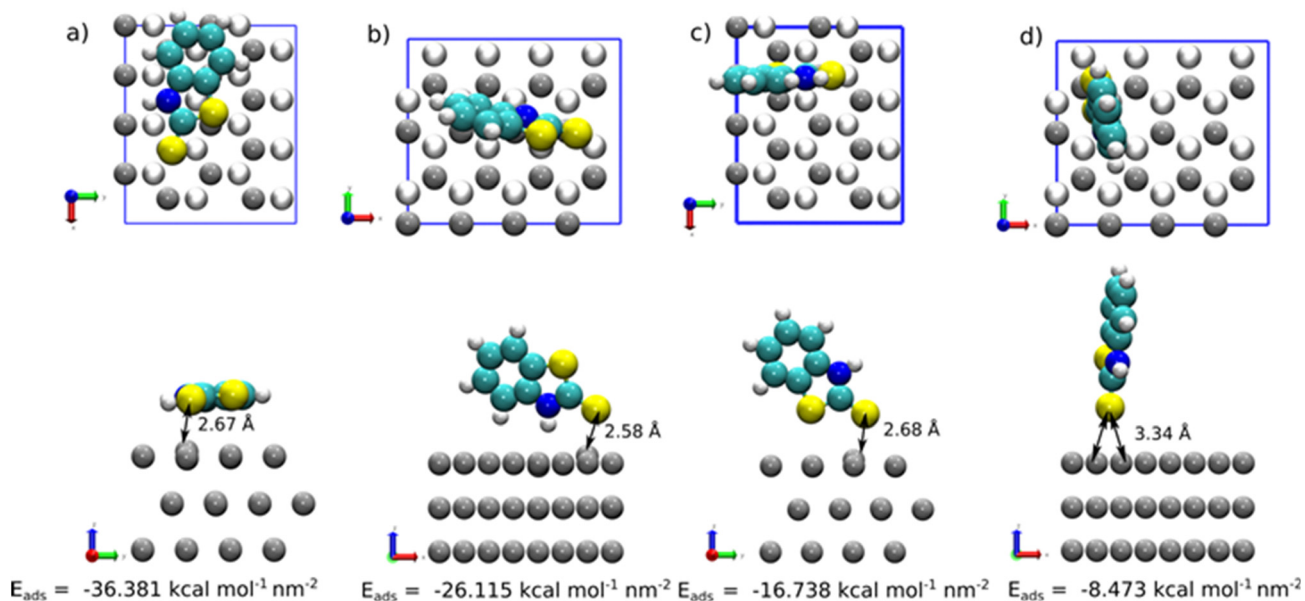

Fig. 8 Top view and side view of the final adsorption structures at low concentration (1 molecule per nm² obtained for 2-MBT on Zn{0001}: (a) parallel, (b) (S,NH)-Zn, (c) (S,S)-Zn, and (d) (S)-Zn cases. White, cyan, yellow, blue, and gray colored spheres represent H, C, S, N, and Zn atoms, respectively. In the top view, degraded color spheres represent the Zn under the surface.

E_{ads} = -36.381 kcal mol^{-1} nm^{-2} E_{ads} = -26.115 kcal mol^{-1} nm^{-2} E_{ads} = -16.738 kcal mol^{-1} nm^{-2} E_{ads} = -8.473 kcal mol^{-1} nm^{-2}
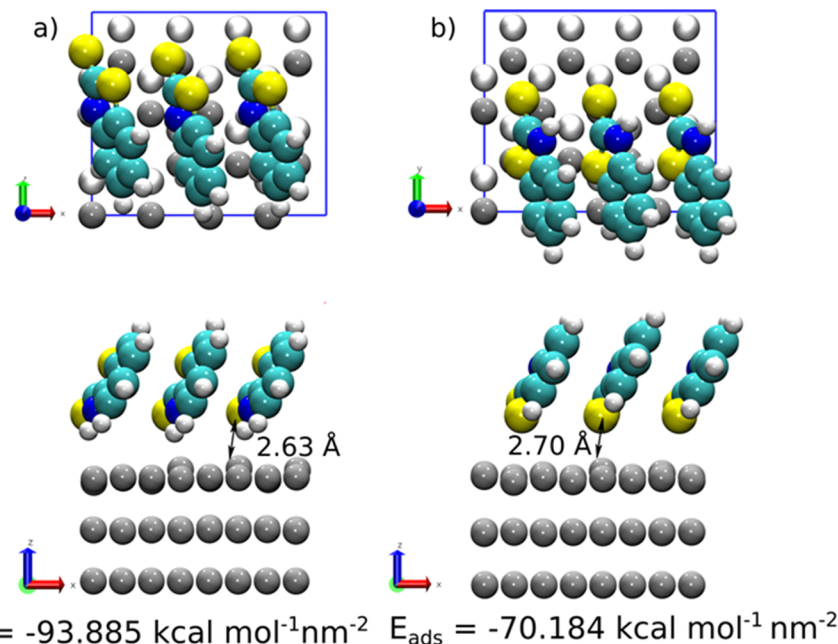
Fig. 9 Top view and side view for the final adsorption structures at high concentration (3 molecules per nm^2 obtained for 2-MBT on Zn{0001}: a) (S,NH)-Zn, and b) (S,S)-Zn cases. White, cyan, yellow, blue, and gray colored spheres represent H, C, S, N, and Zn atoms, respectively. On the top view of each case, degraded color spheres represent the Zn under the surface.

Adsorption stability and film growth at polarised ZE surfaces

To determine the inhibitor film stability and its growth/ degradation kinetics, the ZE/solution interface was polarised at different applied potentials (0 to +75 mV $vs.$ free corrosion potential). The applied overpotential aims to increase ZE corrosion kinetics. Prior to polarisation, ZE was immersed in the inhibited solution for 90 min to generate inhibitor film as well as achieve quasi-stationarities of the electrochemical system. Then, the applied overpotential was held for 2 h to record the variation of current densities of ZE as a function of time. Fig. 10 illustrates the effect of polarisation of each inhibitor case in contrast to the uninhibited counterparts.

For ZE in plain NaCl solution, it is shown that current density increases with increasing applied overpotential, essentially due to the enlarged potential drop accelerating corrosion. In contrast, the addition of either inhibitor molecule reduces current densities to different degrees by the presence of inhibitive film. In the case of 2-ABT, at an overpotential of +25 mV, the current densities show a significantly low magnitude, indicating that 2-ABT inhibitor film remains effective in protecting the underlying ZE from corrosion. As the overpotential increases to +50 mV, the inhibitor film appears to partly dissociate from the interface where current densities start to increase with potential hold. At +75 mV, current densities show nearly the same magnitude of increase as the uninhibited ZE, reflecting that
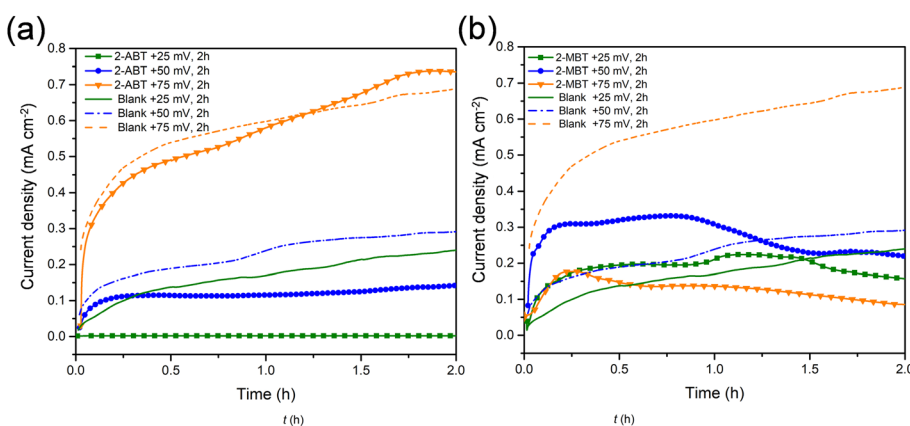
Fig. 10 Variation of current densities of ZE interface as a function of time under different applied overpotentials in the inhibitor (1 mM)-containing NaCl solution. (a) 2-ABT and (b) 2-MBT.
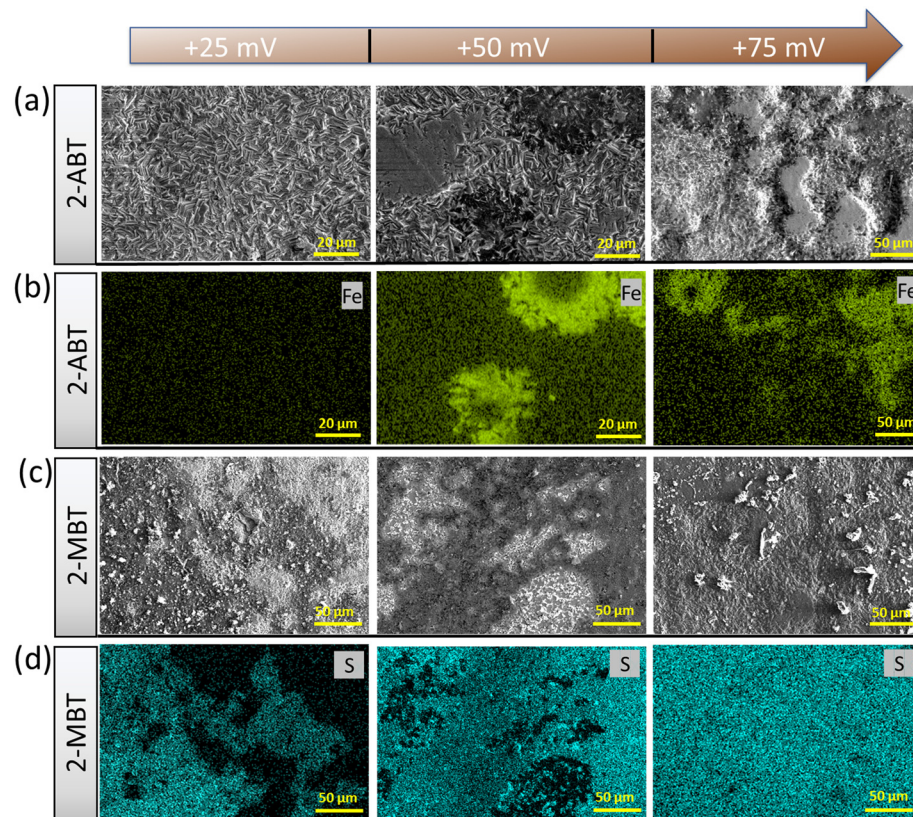
Fig. 11 Surface morphology of ZE surface at different potential holds for 2 h in NaCl solution in the presence of 1 mM candidate inhibitor. SEM images for (a) 2-ABT and (c) 2-MBT. (b and d) EDX mapping of each potential hold case of (a) and (c), respectively.

the inhibiting effect is significantly reduced relative to the depletion of adsorbed inhibition film.

Differing from 2-ABT, a rapid increase in current densities greater than that of the uninhibited counterpart was observed for 2-MBT at the initial stage under overpotentials of both +25 mV and +50 mV (Fig. 10b). This can be ascribed to the fact that in the presence of inhomogeneous 2-MBT film there would be decreased metal exposure area (Fig. 11), which leads to increased corrosion current density. However, a change in corrosion kinetics with the held potentials should be noted. At +25 mV, a reduction of current density was recorded at approx. 1.5 h, after which point the value is lower than that of the uninhibited solution. A similar observation was also made for the case of +50 mV after a potential hold of approx. 1.2 h. It can be related to the fact that corrosion activity was enhanced with polarisation which gives rise to increased concentration of Zn^{2+} at the proximity of the ZE interface. This process promotes more inhibitor precipitate formation upon ZE, mitigating further corrosion. This is further confirmed when the overpotential was increased to +75 mV, where greatly decreased current densities were revealed, signifying more effective surface protection with time once the potential was applied.

Further evidence was provided by acquiring the surface morphology of polarised ZE surfaces under different applied overpotentials after immersion in the inhibited solution. For

2-ABT, at an overpotential of +25 mV the ZE surface is mostly intact as the adsorbed inhibitor film is preserved. As overpotential increases, Zn dissolution takes place where localised corrosion becomes more evident (Fig. 11a). EDX mapping also reveals an enhanced Fe signal originating from the steel substrate where Zn is depleted, reflecting that the inhibitor film is gradually displaced under these conditions (Fig. 11b).

On the other hand, polarisation plays a beneficial role in the film/layer growth for the case of 2-MBT due to its complexation ability. As evidenced in Fig. 11c and d, with the increase of overpotential the inhibitor film/layer becomes more densified, affording a more general surface coverage. Fig. 12 reveals the cross-sectional structure of the protective layer formed at +75 mV, which demonstrates a compact inner layer and an outer layer with internal voiding. This is pertinent to the aforementioned film growth kinetics, in which the precipitation process gives rise to large thickness (~2 μm) and less porosity of the initially formed layer. This would also promote formation of corrosion products on account of less spatial separation of the anodic and cathodic reactions.[46] As the layer builds up, Zn^{2+} diffuses through the defects at the liquid boundary, further favouring rapid precipitation at high ion concentration. This phenomenon has also been reported by Cole et al., who studied the corrosion product formation of zinc under a droplet as a

This journal is © The Royal Society of Chemistry and IChemE 2024

Mol. Syst. Des. Eng., 2024, **9**, 29–45 | **41**
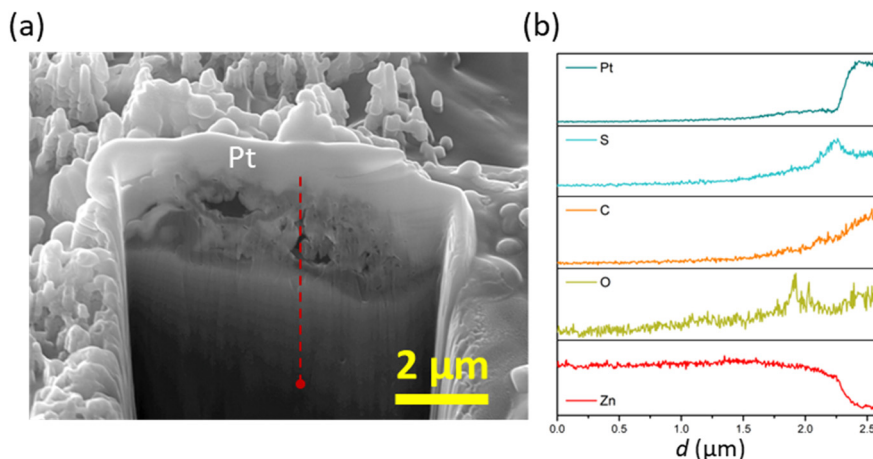
Fig. 12 Cross-sectional morphology and elemental distribution of ZE specimen after 2 h polarisation (+75 mV) in the inhibited solution of 1 mM 2-MBT. (a) FIM-SEM image; (b) EDX line scan of the area of interest marked by dotted lines in (a).
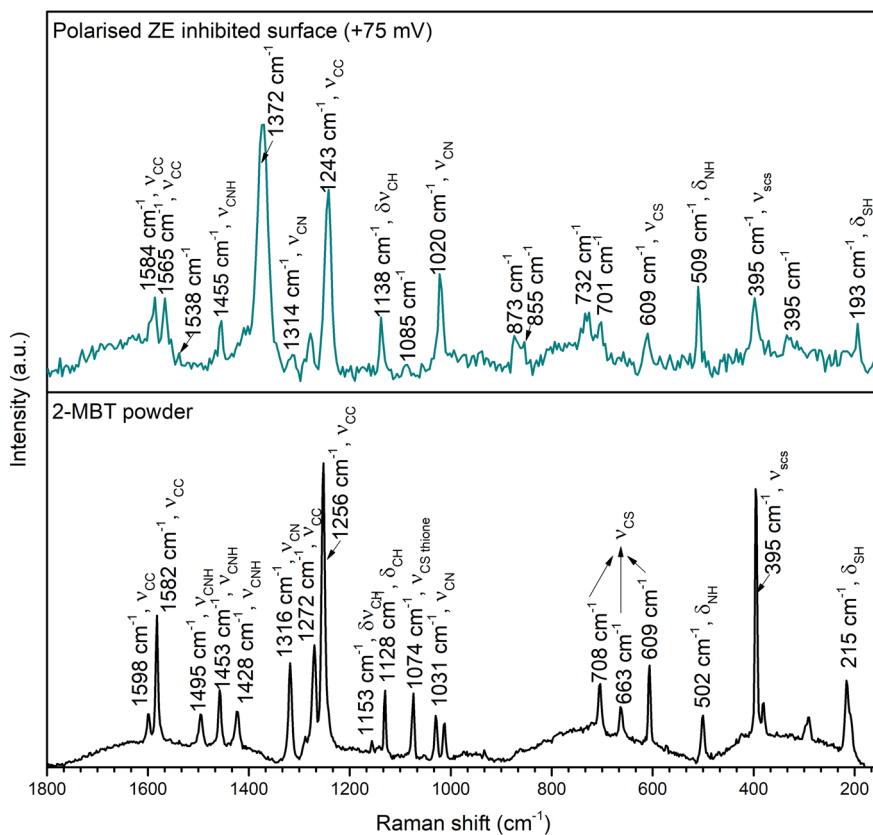
Fig. 13 Raman spectra of 2-MBT powder and ZE inhibited surface after 2 h polarisation in the inhibited solution of 1 mM 2-MBT.

function of time and described it as a "volcano effect".[47] This is further supported by EDX results, where increased concentration of S originating from the inhibitor molecule was displayed, denoting the participation of 2-MBT in the layer formation. In addition, abundant signals of O were noted, presumably by the stabilised corrosion products with OH^- and/or CO_3^{2+} of the precipitate layer.

To elaborate on the nature of the formed product layer upon polarised ZE surfaces, Raman spectrometry was

conducted to resolve the chemical bonds of the precipitates. Fig. 13 presents the Raman spectra of 2-MBT chemical powder and the inhibited ZE surface after 2 h polarisation at +75 mV. The Raman spectra of ZE at different overpotentials are also documented in Fig. S7,† which show identical chemical environments. For 2-MBT powder, the bands observed at 1598, 1582, and 1272 cm^{-1} are associated with the C=C stretching mode of the aromatic ring.[48] The peak centred at 215 cm^{-1} is ascribed to the bending mode of S–

42 | *Mol. Syst. Des. Eng.*, 2024, **9**, 29–45

This journal is © The Royal Society of Chemistry and IChemE 2024

H.[48,49] The stretching vibrations of C–N–H(1495, 1453 and 1428 cm^{-1}) were also recorded, and C=S stretching mode was observed at 1074 cm^{-1}.[50]

The presence of the characteristic peaks of the inhibitor molecule on the inhibited ZE surface confirms that 2-MBT contributes to the product layer formation. It was observed that certain peaks were downshifted and broadened as a result of the chemical bonding with the metal.[51,52] In particular, the peaks associated with $v_{(C–N–H)}$, $v_{(S–H)}$ and $v_{(C–S)}$ greatly declined, which can be attributed to the interaction between these functionalities with Zn. Indeed, XPS results have also confirmed that the thiol group and endocyclic N act as reaction sites with Zn. It is also worth noting that certain peaks non-related to 2-MBT were recorded at 1372, 1085, 732, 701 and 395 cm^{-1}, possibly originating from other corrosion products. Determining the nature of corrosion products with precise peak correlation is not straightforward, obscured by overlaying peaks and the possible coordination of inhibitor molecules. Nonetheless, the main peak positioned at 1085 cm^{-1} coincides with symmetric stretching of CO$_3^{2-}$. Correspondingly, the observed peak at 1538 cm^{-1} could be associated with the asymmetric vibration mode of zinc carbonate or hydrozincite – the latter is more likely as indicated by the characteristic peaks of bending mode at 701 and 732 cm^{-1}.[53,54] The weak peak at 395 cm^{-1} could be assigned to Zn(OH)$_2$, although the presence of ZnO can be hardly confirmed with the increasing background noise in the region between 440 and 560 cm^{-1}.[53,55] Despite the correlation being less definitive, the presence of these identified peaks agrees with the EDX analysis (Fig. 10b) in which increasing O concentration at the product layer is due to the presence of OH$^-$ and/or CO$_3^{2-}$.

Mechanism of inhibition

The exploration of benzothiazole and its derivatives as promising corrosion inhibitors has been receiving increasing attention, with attempts to further refine the mechanistic understanding of metal–molecule interaction and thereafter direct molecular tailoring for enhanced inhibition performance. To this end, this study provides further insights into different inhibition modes of action of two substituted benzothiazoles, i.e., 2-ABT and 2-MBT, towards the ZE surface under a saline environment.

Both candidates act as corrosion inhibitors for ZE against short-term corrosion. For 2-ABT, a homogenous inhibitor film is formed upon the metal surface in which chemisorbed 2-ABT molecules via endocyclic S contribute to effective surface protection, mitigating the charge transfer process at the metal–solution interface. The attached amino group with a delocalised electron pair conjugates with the heterocycle, potentially influencing the electronic environment of heterocyclic S to interact with the vacant orbital of Zn.[56] Similarly, it would be assumed that inhibitor candidate 2-MBT with the thiol group possessing free pairs of electrons would provide comparable inhibition performance. In fact,

the theoretical calculations reveal that the adsorption of 2-MBT is energetically stronger than that of 2-ABT at identical concentration levels, supposedly affording higher inhibition efficacy. DFT simulations also indicate that for both inhibitors the increasing concentration gives rise to higher adsorption stability, in which inhibitor molecules are directed in a tilted position under saturated conditions with enhanced interaction between the presented heteroatom(s) and the anchored Zn atom.

Noticeably, it is observed from DFT results that the strong interaction between 2-MBT and Zn leads to the larger displacement of the targeting Zn atom, which is further enhanced at greater adsorption coverage. It is worth noting that, in actual corrosive medium, exposed fresh Zn surface is free-corroded with metal ions readily released at the metal–solution interface. Therefore, intense metal–inhibitor interaction for reactive substrates such as Zn and galvanised steel may cause further metal dissolution instead of immediate surface protection. Indeed, in our study, Zn/2-MBT coordination complexes (via ar. N and exo S) were detected in the solution. Nonetheless, the coordinated components contribute to the product formation by precipitating subsequently upon the metal surface. This has also been suggested by both SEM and XPS results where the precipitated Zn/2-MBT species were confirmed on the inhibited ZE surface after immersion. The determined adsorption mechanism differs from that of 2-ABT, in which the high basicity of the amino group in 2-ABT is less favourable as the coordination site.[57] Furthermore, as indicated by the simulation results, the H atoms in the NH$_2$ group of 2-ABT seem to play a repulsive role with the surface supposedly mitigating abstraction of the Zn atom from the surface as compared to 2-MBT.

With different adsorption behaviour clarified for both inhibitor molecules, the adsorption stability and film growth/degradation mechanisms were further studied. Fig. 14 illustrates the inhibitor film formation and evolution at polarised ZE surfaces. At a small surface potential increase (+25 mV), the inhibition film of 2-ABT remains effective as a result of stable chemical adsorption. With elevated surface potential, chemisorbed 2-ABT molecules dissociate from the metal interface, leading to insufficient surface protection. Nonetheless, owing to the complexation ability of 2-MBT, with increased Zn^{2+} release at the interface of higher overpotentials more compact product layer was generated, reinforcing corrosion performance. The determined distinct inhibition behaviour of 2-MBT is also potentially useful for applications such as Zn coating self-repair where coating damage may lead to such potential drops as well as galvanising surface modification by electrochemical treatment.

Conclusion

The inhibitory behaviours and adsorption stability of two substituted benzothiazoles (2-ABT and 2-MBT) against ZE

This journal is © The Royal Society of Chemistry and IChemE 2024

Mol. Syst. Des. Eng., 2024, 9, 29–45 | 43
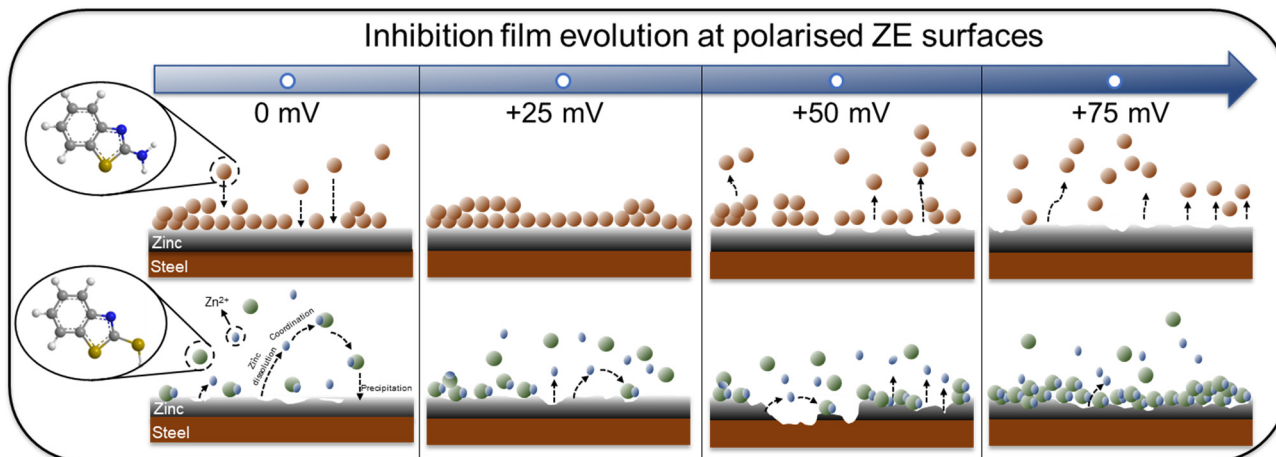
Fig. 14 Schematic illustration of inhibition film formation and sustainability at the ZE surface with surface overpotentials ranging from 0 to +75 mV.

corrosion were studied to determine the intricate role of molecular structural change on the inhibition property. Electrochemical results show that both candidate molecules are mixed-type inhibitors reducing both anodic and cathodic corrosion reactions of ZE. An inhibition efficiency of 81% and 77% at a concentration of 1 mM was determined by PDS for 2-MBT and 2-ABT, respectively. EIS results suggest that the interfacial state of 2-MBT differs from that of 2-ABT, comprising two relaxation processes associated with a different interfacial condition. Surface analysis exhibits "island-shaped" micro-sized inhibitor products precipitated upon ZE in the presence of 2-MBT, whilst the pristine feature of ZE remains in the case of 2-ABT due to thin inhibitor film formation. As revealed by XPS analysis, 2-ABT promotes chemisorption *via* endo S as the adsorption site, while 2-MBT is able to chelate with released Zn^{2+} in solution by endo N and S_{thiol} which thereafter contributes to inhomogeneous product precipitation upon ZE. Density functional theory (DFT) results reveal that whilst at low inhibitor concentration the adsorbed molecule in a parallel position renders high stability *via* π–π interaction, at high concentration the adsorption becomes more stable in tilted configuration with heteroatoms directed towards the metal. Between 2-MBT and 2-ABT, 2-MBT was shown to interact more strongly with the Zn surface. Remarkably, the displacement of the Zn surface atom in the presence of 2-MBT molecules was displayed, which provides further evidence of the formation of the Zn/2-MBT complex in aqueous medium. The inhibition performance determined upon the polarised ZE surface shows that 2-ABT remains effective at low overpotential. With potential increase, the inhibitor molecules of 2-ABT dissociate from the metal surface, compromising the inhibition performance. In contrast, owing to the coordination ability of 2-MBT, a more condensed product layer is facilitated at greater Zn^{2+} release at increasing potentials, affording inhibition improvement. This study is anticipated to provide new knowledge and insight for rational inhibitor engineering to realise tailored corrosion inhibition properties.

Conflicts of interest

There are no conflicts to declare.

References

1 M. Iannuzzi and G. S. Frankel, *npj Mater. Degrad.*, 2022, **6**, 101.

2 M. M. Kadhim, A. A. Khadom, A. Mahdi Rheima and H. Abdulkareem Almashhadani, *J. Mol. Liq.*, 2023, **377**, 121538.

3 L. Wang, H. Wang, A. Seyeux, S. Zanna, A. Pailleret, S. Nesic and P. Marcus, *Corros. Sci.*, 2023, **213**, 110952.

4 L. Liu, Q. Deng, P. White, S. Dong, I. S. Cole, J. Dong and X.-B. Chen, *Corros. Commun.*, 2022, **8**, 40–48.

5 R. Aslam, M. Mobin, S. Zehra and J. Aslam, *J. Mol. Liq.*, 2022, **364**, 119992.

6 E. Vernack, D. Costa, P. Tingaut and P. Marcus, *Corros. Sci.*, 2020, **174**, 108840.

44 | *Mol. Syst. Des. Eng.*, 2024, **9**, 29–45

This journal is © The Royal Society of Chemistry and IChemE 2024

7 S. B. Sharma, V. Maurice, L. H. Klein and P. Marcus, *J. Electrochem. Soc.*, 2020, **167**, 161504.

8 H. A. Mohamed, A. A. Farag and B. M. Badran, *J. Appl. Polym. Sci.*, 2010, **117**, 1270–1278.

9 A. C. Balaskas, M. Curioni and G. E. Thompson, *Surf. Interface Anal.*, 2015, **47**, 1029–1039.

10 Z. Liu, B. Fan, J. Zhao, B. Yang and X. Zheng, *Corros. Sci.*, 2023, **212**, 110957.

11 W. Li, T. Ma, B. Tan, S. Zhang, M. Yan, J. Ji, F. Wang, H. Du and X. Wang, *Colloids Surf., A*, 2022, **649**, 129531.

12 F. Chiter, D. Costa, V. Maurice and P. Marcus, *Appl. Surf. Sci.*, 2021, **537**, 147802.

13 F. Chiter, D. Costa, V. Maurice and P. Marcus, *npj Mater. Degrad.*, 2021, **5**, 52.

14 M. Finšgar and D. Kek Merl, *Corros. Sci.*, 2014, **83**, 164–175.

15 X. Wu, F. Wiame, V. Maurice and P. Marcus, *Corros. Sci.*, 2020, **166**, 108464.

16 X. Wu, F. Wiame, V. Maurice and P. Marcus, *Appl. Surf. Sci.*, 2020, **508**, 145132.

17 M. Finšgar and D. Čakara, *Appl. Surf. Sci.*, 2022, **606**, 154843.

18 X. Wu, F. Wiame, V. Maurice and P. Marcus, *Corros. Sci.*, 2021, **189**, 109565.

19 V. Garg, S. B. Sharma, S. Zanna, A. Seyeux, F. Wiame, V. Maurice and P. Marcus, *Electrochim. Acta*, 2023, **447**, DOI: **10.1016/j.electacta.2023.142162**.

20 Q. Deng, S. Jeschke, B. J. Murdoch, S. Hirth, P. Eiden, J. N. Gorges, P. Keil, X.-B. Chen and I. Cole, *Corros. Sci.*, 2022, **199**, 110206.

21 E. Artacho, E. Anglada, O. Diéguez, J. D. Gale, A. García, J. Junquera, R. M. Martin, P. Ordejón, J. M. Pruneda, D. Sánchez-Portal and J. M. Soler, *J. Phys.: Condens. Matter*, 2008, **20**, 064208.

22 A. García, N. Papior, A. Akhtar, E. Artacho, V. Blum, E. Bosoni, P. Brandimarte, M. Brandbyge, J. I. Cerdá, F. Corsetti, R. Cuadrado, V. Dikan, J. Ferrer, J. Gale, P. García-Fernández, V. M. García-Suárez, S. García, G. Huhs, S. Illera, R. Korytár, P. Koval, I. Lebedeva, L. Lin, P. López-Tarifa, S. G. Mayo, S. Mohr, P. Ordejón, A. Postnikov, Y. Pouillon, M. Pruneda, R. Robles, D. Sánchez-Portal, J. M. Soler, R. Ullah, V. W.-Z. Yu and J. Junquera, *J. Chem. Phys.*, 2020, **152**, 204108.

23 M. S. José, A. Emilio, D. G. Julian, G. Alberto, J. Javier, O. Pablo and S.-P. Daniel, *J. Phys.: Condens. Matter*, 2002, **14**, 2745.

24 J. P. Perdew, K. Burke and M. Ernzerhof, *Phys. Rev. Lett.*, 1996, **77**, 3865–3868.

25 A. Jain, S. P. Ong, G. Hautier, W. Chen, W. D. Richards, S. Dacek, S. Cholia, D. Gunter, D. Skinner, G. Ceder and K. A. Persson, *APL Mater.*, 2013, **1**, 011002.

26 E. Anglada, J. M. Soler, J. Junquera and E. Artacho, *Phys. Rev. B: Condens. Matter Mater. Phys.*, 2002, **66**, 205101.

27 S. García-Gil, A. García, N. Lorente and P. Ordejón, *Phys. Rev. B: Condens. Matter Mater. Phys.*, 2009, **79**, 075441.

28 N. Troullier and J. L. Martins, *Phys. Rev. B: Condens. Matter Mater. Phys.*, 1991, **43**, 1993–2006.

29 M. J. van Setten, M. Giantomassi, E. Bousquet, M. J. Verstraete, D. R. Hamann, X. Gonze and G. M. Rignanese, *Comput. Phys. Commun.*, 2018, **226**, 39–54.

30 A. García, M. J. Verstraete, Y. Pouillon and J. Junquera, *Comput. Phys. Commun.*, 2018, **227**, 51–71.

31 S. Grimme, *J. Comput. Chem.*, 2006, **27**, 1787–1799.

32 E. McCafferty, *Corros. Sci.*, 2005, **47**, 3202–3215.

33 M. P. Desimone, G. Grundmeier, G. Gordillo and S. N. Simison, *Electrochim. Acta*, 2011, **56**, 2990–2998.

34 S. J. Garcia, T. A. Markley, J. M. C. Mol and A. E. Hughes, *Corros. Sci.*, 2013, **69**, 346–358.

35 A. V. Benedeti, P. T. A. Sumodjo, K. Nobe, P. L. Cabot and W. G. Proud, *Electrochim. Acta*, 1995, **40**, 2657–2668.

36 J. Li, C. W. Du, Z. Y. Liu, X. G. Li and M. Liu, *Int. J. Electrochem. Sci.*, 2016, **11**, 10690–10705.

37 S. Sheetal, M. Sengupta, S. Singh, B. Thakur, P. Pani, S. Kaya Banerjee and A. K. Singh, *J. Mol. Liq.*, 2022, **354**, 118890.

38 C. E. Mitchell, D. Santos-Carballal, A. M. Beale, W. Jones, D. J. Morgan, M. Sankar and N. H. de Leeuw, *Faraday Discuss.*, 2021, **230**, 30–51.

39 R. V. Siriwardane and J. A. Poston, *Appl. Surf. Sci.*, 1990, **45**, 131–139.

40 M. Wang, B. Fan, B. Wen and C. Jiang, *Sci. China: Technol. Sci.*, 2020, **63**, 2098–2112.

41 C. M. Whelan, M. R. Smyth, C. J. Barnes, N. M. D. Brown and C. A. Anderson, *Appl. Surf. Sci.*, 1998, **134**, 144–158.

42 E. Vernack, S. Zanna, A. Seyeux, D. Costa, F. Chiter, P. Tingaut and P. Marcus, *Corros. Sci.*, 2023, **210**, 110854.

43 A. L. R. Silva and M. D. M. C. Ribeiro da Silva, *J. Therm. Anal. Calorim.*, 2017, **129**, 1679–1688.

44 L. P. Kazansky, I. A. Selyaninov and Y. I. Kuznetsov, *Appl. Surf. Sci.*, 2012, **258**, 6807–6813.

45 G. Liu, Y. Huang, X. Qu, J. Xiao, X. Yang and Z. Xu, *Colloids Surf., A*, 2016, **503**, 34–42.

46 M. S. Venkatraman, I. S. Cole and B. Emmanuel, *Electrochim. Acta*, 2011, **56**, 8192–8203.

47 I. S. Cole, T. H. Muster, S. A. Furman, N. Wright and A. Bradbury, *J. Electrochem. Soc.*, 2008, **155**, C244.

48 N. Sandhyarani, G. Skanth, S. Berchmans, V. Yegnaraman and T. Pradeep, *J. Colloid Interface Sci.*, 1999, **209**, 154–161.

49 W. Sąsiadek, I. Bryndal, M. Ptak, R. Lisiecki, T. Lis and J. Hanuza, *J. Mol. Struct.*, 2023, 135531.

50 A. K. Rai, R. Singh, K. N. Singh and V. B. Singh, *Spectrochim. Acta, Part A*, 2006, **63**, 483–490.

51 M. H. Shahini, M. Keramatinia, M. Ramezanzadeh, B. Ramezanzadeh and G. Bahlakeh, *J. Mol. Liq.*, 2021, **342**, 117570.

52 P. Vashishth, H. Bairagi, R. Narang, S. K. Shukla and B. Mangla, *J. Mol. Liq.*, 2022, **365**, 120042.

53 I. S. Cole, T. H. Muster, D. Lau, N. Wright and N. S. Azmat, *J. Electrochem. Soc.*, 2010, **157**, C213.

54 M. C. Hales and R. L. Frost, *Polyhedron*, 2007, **26**, 4955–4962.

55 A. H.-L. Goff, S. Joiret, B. Saïdani and R. Wiart, *J. Electroanal. Chem. Interfacial Electrochem.*, 1989, **263**, 127–135.

56 I. Danaee, M. Gholami, M. RashvandAvei and M. H. Maddahy, *J. Ind. Eng. Chem.*, 2015, **26**, 81–94.

57 J. Lopes de Miranda, B. Lages Rodrigues, L. Cristina de Moura, G. Sales da Rocha and S. de Sant'Ana Oliveira, *Results Chem.*, 2023, **5**, 100785.

This journal is © The Royal Society of Chemistry and IChemE 2024

Mol. Syst. Des. Eng., 2024, **9**, 29–45 | **45**